ADVANCED ENGINEERING MATERIALS
www.aem-journal.com

Effect of Cerium Addition on the Microstructure and Shape Memory Properties of Austenitic Fe–Mn–Si–Cr–Ni Alloys

Rodrigo da Silva, Luis Felipe Sverzut Baroni, Claudio Bessera Martins Junior, Danielle Cristina Camilo Magalhães, Guilherme Santos Vacchi, Andrea Madeira Kliauga, Nelson Batista Lima, Jorge Otubo, and Carlos Alberto Della Rovere**

The addition of rare earth elements, such as cerium, to austenitic Fe–Mn–Si-based shape memory alloys has been shown to improve both corrosion resistance and shape recovery. However, the mechanisms underlying the effect of Ce on shape recovery are still unclear. This study investigates the influence of the addition of small amounts of Ce (0.18, 0.42, and 0.96 wt%) on the microstructure and shape recovery of an austenitic Fe–13.50Mn–3.98Si–9.54Cr–4.51Ni alloy. Ce additions induce the formation of a large number of Ce-rich particles, which act as austenitic grain refiners. Both grain refinement and the formation of Ce-rich particles contribute to the strengthening of the matrix at 0.42 wt% Ce addition. In addition, Ce additions alter the M_S temperature, which increases with Ce additions. Total shape recovery improves with 0.18 and 0.42 wt% Ce additions, but decreases with 0.96 wt% Ce addition. The beneficial effect of Ce addition in improving the shape recovery of the austenitic Fe–Mn–Si–Cr–Ni alloy is related to the enhancement of the elastic shape recovery component of the total shape recovery. However, the shape memory recovery due to the shape memory effect always decreases with the increase of the Ce content.

1. Introduction

Austenitic Fe–Mn–Si–Cr–Ni alloys combine the properties of austenitic stainless steel, such as good formability and enhanced wear and corrosion resistance, with the ability to recovery its original shape when deformed under certain conditions, a phenomenon known as the shape memory effect (SME).[1] This effect results from the reverse transformation of the nonthermoelastic ε-martensite hexagonal close-packed (HCP) to the parent γ-austenite face-centered cubic (FCC) phase by Shockley partial dislocation motions.[2,3]

To achieve higher SME values, the most common and effective method is to impose repeated cycles of $\gamma \leftrightarrow \varepsilon$ transformation, known as training, which reduces the critical stress for martensite formation[4] and introduces a degree of uniformity in distribution of the pre-existing stacking faults (SFs) in austenite.[5] However, this series of thermomechanical processes increases the complexity and the cost of production. Since many metallurgical aspects (such as grain refinement, presence of precipitates, occurrence of α'-martensite body-centered cubic [BCC] and stacking fault energy [SFE]) are involved in the outcome of total shape recovery (TSR) and are controlled by alloy design and processing, the understanding of SME mechanisms has enabled other ways to achieve higher shape recovery. Previous studies[6–11] have shown that additions of certain alloying elements (Si, Ce, Nb, Ti, C, V, N etc.) can promote strengthening of the austenitic phase by solid solution, grain refinement, and/or second-phase hardening. It has been suggested that austenite phase strengthening may allow higher stresses to be applied, facilitating stress-induced ε-martensite transformation without causing permanent slip.

In this context, the Ce addition has been studied over the past decades and has been shown to be a relatively low-cost alternative to improve the TSR of Fe–Mn–Si–Cr–(Ni) shape memory alloy (SMAs). TSR is the sum of the components involved in shape recovery, elastic shape recovery (ESR), and shape memory recovery (SMR) due to SME. However, the main role of Ce addition in

R. Silva, L. F. S. Baroni, C. B. Martins Junior, D. C. Camilo Magalhães, G. S. Vacchi, C. A. Della Rovere
Munir Rachid Corrosion Laboratory
Department of Materials Engineering
Federal University of São Carlos
Rodovia Washington Luis Km 235, São Carlos 13.565-905, SP, Brazil
E-mail: rsilva@ufscar.br; rovere@ufscar.br

R. Silva, C. B. Martins Junior, A. M. Kliauga, C. A. Della Rovere
Graduate Program in Materials Science and Engineering
Federal University of São Carlos

N. B. Lima, J. Otubo
Nuclear and Energy Research Institute - IPEN
São Paulo 05508-000, SP, Brazil

J. Otubo
Division of Mechanical Engineering
Technological Institute of Aeronautics
São José dos Campos 12228-900, SP, Brazil

The ORCID identification number(s) for the author(s) of this article can be found under https://doi.org/10.1002/adem.202301513.

DOI: 10.1002/adem.202301513

improving shape recovery is unclear in the literature. It has been proposed that Ce additions can promote beneficial changes for SME such as SFE reduction and austenitic phase strengthening.[6,12,13] The reduction in SFE with Ce additions is due to a chemical interaction that promotes the segregation of Ce atoms in the SFs, significantly reducing the SFE (the so-called Suzuki effect).[14,15] However, since Ce solubility in Fe-based systems is extremely low,[16] its contribution to the reduction of SFE is limited. Thus, the strengthening of the austenitic phase appears to be the main factor acting on the TSR improvement. This is the result of the formation of Ce-rich particles leading to grain refinement and/or second-phase hardening.

However, the improvement of SME through austenitic phase strengthening promoted by grain refinement is currently being questioned. Recent studies reported by Wang et al.[17] and Yong et al.[18] have shown that grain refinement increases the constraining effects of grain boundaries and annealing twins on the stress-induced martensitic transformation and supports plastic deformation, thereby reducing SME. In addition, Käfer et al.[19,20] showed that the improvement in TSR with austenitic phase strengthening due to grain refinement and precipitate formation primarily comes from ESR instead of SMR. These findings cast doubt on the role of Ce in improving the shape recovery of Fe–Mn–Si–Cr–(Ni) SMAs, and further studies are needed to clarify its influence.

Therefore, this study aims to understand the effect of Ce on the microstructure and SME of austenitic Fe–13.50Mn–4Si–9.5Cr–4.5Ni SMA. The composition chosen for Ce additions showed a significant improvement in aqueous and high-temperature corrosion resistance with the addition of this element.[21,22] These improvements make this material a potential candidate for pipe couplings that can be used in engineering applications requiring corrosion-resistant materials. Since previous studies[12,13,23] have reported an improvement in the SME of Fe–Mn–Si–Cr–(Ni) SMAs with additions of up to 0.64 wt% of rare earth elements (REE), Ce additions of 0.18, 0.42, and 0.96 wt% were made to evaluate the microstructural changes as a function of Ce content and its influence on the SME. In order to distinguish the phenomena involved in the TSR, the contributions of ESR and SMR leading to TSR were analyzed separately.

1.1. Experimental Section

Fe–13.50Mn–4Si–9.5Cr–4.5Ni SMA was cast in a vacuum induction melting furnace with a saturated argon atmosphere, using AISI 304L stainless steel bars as the raw material and the chemical composition adjusted with additions of high-purity Fe, Mn, Si, and Ni. Small amounts of Ce were then added to the Ce-free alloy by casting in a Bühler model arc-melter (AM) electric arc furnace. **Table 1** shows the chemical compositions determined by inductively coupled plasma–optical emission spectrometry. Carbon (C) and sulfur (S) contents were quantified by combustion using a LECO CS-844 analyzer. These alloys are hereafter referred to as SMA-1, SMA-2, SMA-3, and SMA-4. The buttons were hot rolled at 1000 °C and then solution treated (ST) at 1050 °C for 1 h followed by water quenching.

ST samples were embedded in polyester resin, ground to #1200-grit silicon carbide sandpaper and electrolytically polished in a solution of 95% CH_3COOH + 5% $HClO_4$. Electrolytic polishing was used to remove mechanically induced ε-martensite on the surface during metallographic preparation. The samples were then chemically etched with Villela's reagent (5 mL HCl + 1 mL picric acid + 100 mL ethanol), and the resulting microstructures were analyzed using an Olympus BX41M-LED optical microscope (OM). Electron backscatter diffraction (EBSD) analyses were performed to complement the microstructural observations. EBSD was performed using an FEI Inspect S50 scanning electron microscope (SEM) coupled to an energy-dispersive X-ray spectroscopy (EDS) and EBSD detectors. Samples were scanned with a 0.8 μm step size for EBSD and average grain sizes were determined from the EBSD maps. Mechanical strength as a function of Ce content in the alloy was determined using the Vickers hardness test applying a load of 2 kgf and a dwell time of 15 s in a Future-tech FM500 microhardness tester. Means and standard deviations were calculated based on 10 indentations in each sample.

Table 1. Chemical composition of the studied alloys (wt%).

Material	Mn	Si	Cr	Ni	Ce	C	S	Fe
SMA-1	13.50	3.98	9.54	4.51	–	0.029	0.006	Balance
SMA-2	13.47	3.99	9.46	4.57	0.18	0.023	0.007	Balance
SMA-3	13.54	4.01	9.50	4.53	0.42	0.019	0.005	Balance
SMA-4	13.56	3.95	9.57	4.56	0.96	0.022	0.004	Balance

The martensitic and austenitic transition temperatures were determined using differential scanning calorimetry (DSC - TA Instruments model Q100). Thermal cycling was performed from −20 to 200 °C with a rate of 10 °C min^{-1} and the mean values and standard deviation were based on three measurements of each alloy. The phases constituting the microstructure were identified by X-ray diffraction (XRD) using a Shimadzu model XRD-6100 diffractometer, operating with Cu Kα radiation at 40 kV and 30 mA in the 2θ sweep angle range from 40° to 100° with a counting time of 6 s for each 0.02° step at room temperature. Quantitative phase analysis of the XRD results was performed by the Rietveld method using the GSAS-II software.[24]

Bending tests using 1 mm diameter wires extracted by electrical discharge machining in the hot rolling direction were used to assess the shape recovery (TSR = SME + ESR), this procedure has been adopted elsewhere.[11] **Figure 1** shows a schematic view of the bending test. The wires were bent by applying a prestrain

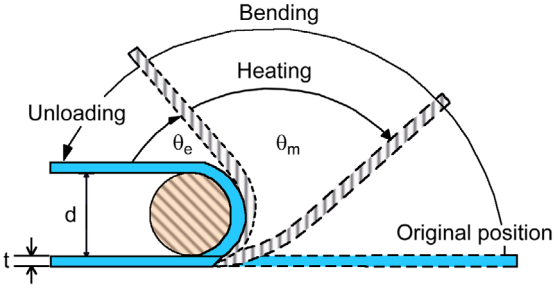

Figure 1. Schematic view of the bending test for assessment of SME.

(PS) load (δ) of 4%, resulting from a 180° bend around a 24 mm-diameter rod (d), as shown in Equation (1).[25,26] Bending was performed in a universal testing machine (Instron 5500R) at room temperature. The shape recovery ratio was determined by measuring the return angles after heating at 600 °C for 10 min based on three measurements of each alloy. TSR was calculated as the sum of ESR and SMR, given by Equation (2)[19] and (3),[1,27] respectively.

$$\delta = \frac{t}{d} \tag{1}$$

$$\mathrm{ESR} = \frac{\theta_e}{180^\circ} \tag{2}$$

$$\mathrm{SMR} = \frac{\theta_m}{(180^\circ - \theta_e)} \tag{3}$$

where δ is the amount of PS, t is the wire diameter (in mm), d is the rod diameter (in mm), θ_e is the angle of ESR upon unloading (in degrees), and θ_m is the angle of SME after austenitic reverse transformation (in degrees) at heating.

Finally, to evaluate the resulting microstructures of the SMAs after deformation, cylindrical samples 6 mm in diameter and 6 mm in length were subjected to 4% compressive strain at room temperature using an Instron 5500R. After the compression tests, the samples were subjected to the same metallographic preparations as above and the constituent phases were characterized by XRD. In addition, light metallographic etching was performed using the Villela reagent and the microstructures were analyzed by SEM.

2. Results

2.1. Microstructural Characterization and Mechanical Strength

Figure 2 shows representative micrographs of the alloys exhibiting microstructures composed of γ-austenite (characterized by annealing twins) and thermal ε-martensite plates formed during water quenching. In SMA-1 (Figure 2a), the microstructure consists of heterogeneous grains with multivariant thermal ε-martensite plates within coarse austenitic grains. In SMA-2 (Figure 2b), the microstructure is finer than that in SMA-1 and consists of both multivariant and monovariant thermal ε-martensite plates within austenitic grains. In SMA-3 (Figure 2c) and SMA-4 (Figure 2d), the austenitic grains are smaller, and some of them contain monovariant ε-martensite plates. However, it is difficult to discern the proportion of grains containing monovariant ε-martensite plates due to the increase in annealing twins with Ce content. In addition, elongated particles are observed at grain boundaries showing a dark contrast due to chemical etching.

For details of the morphology and chemical composition of these particles, backscattered electron (BSE)–SEM images of the polished surfaces of the Ce-containing alloys are shown in **Figure 3**. It is observed that the addition of Ce promotes the formation of particles in the microstructure. The morphology of these particles changes from globular to elongated as the Ce content is increased. EDS spot analysis (results are presented as inset tables) shows that the particles formed in the microstructure of SMA-2, in addition to having high Ce contents, are composed of a mixture of alloying elements, oxygen, and sulfur, with wide

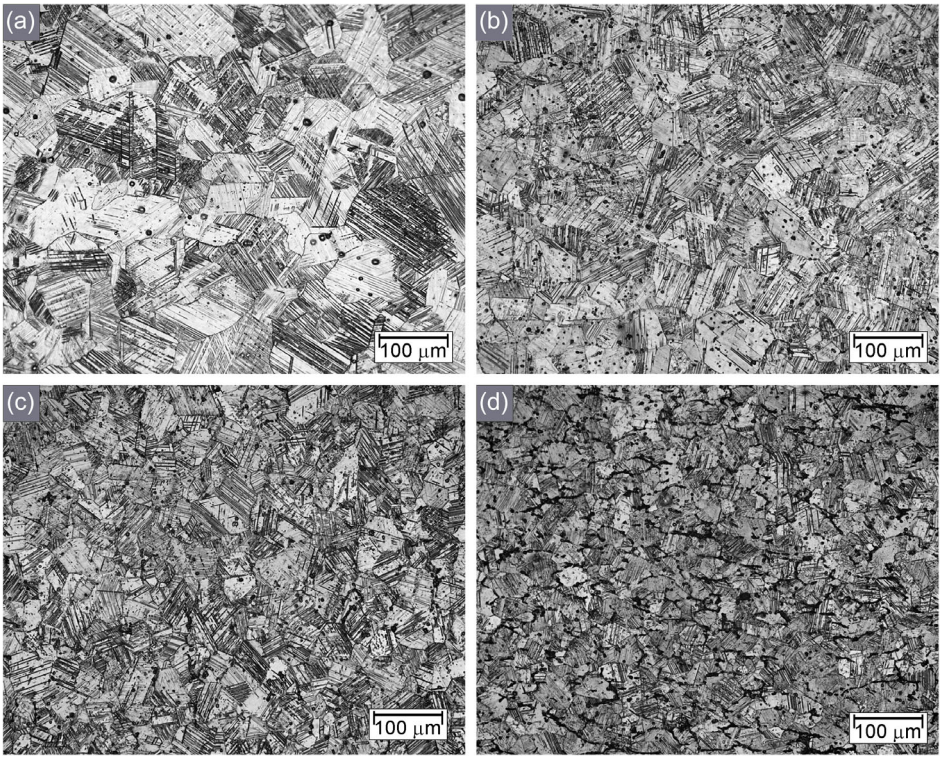

Figure 2. OM images of the resulting microstructure as a function of the Ce addition: a) SMA-1, b) SMA-2, c) SMA-3, and d) SMA-4.

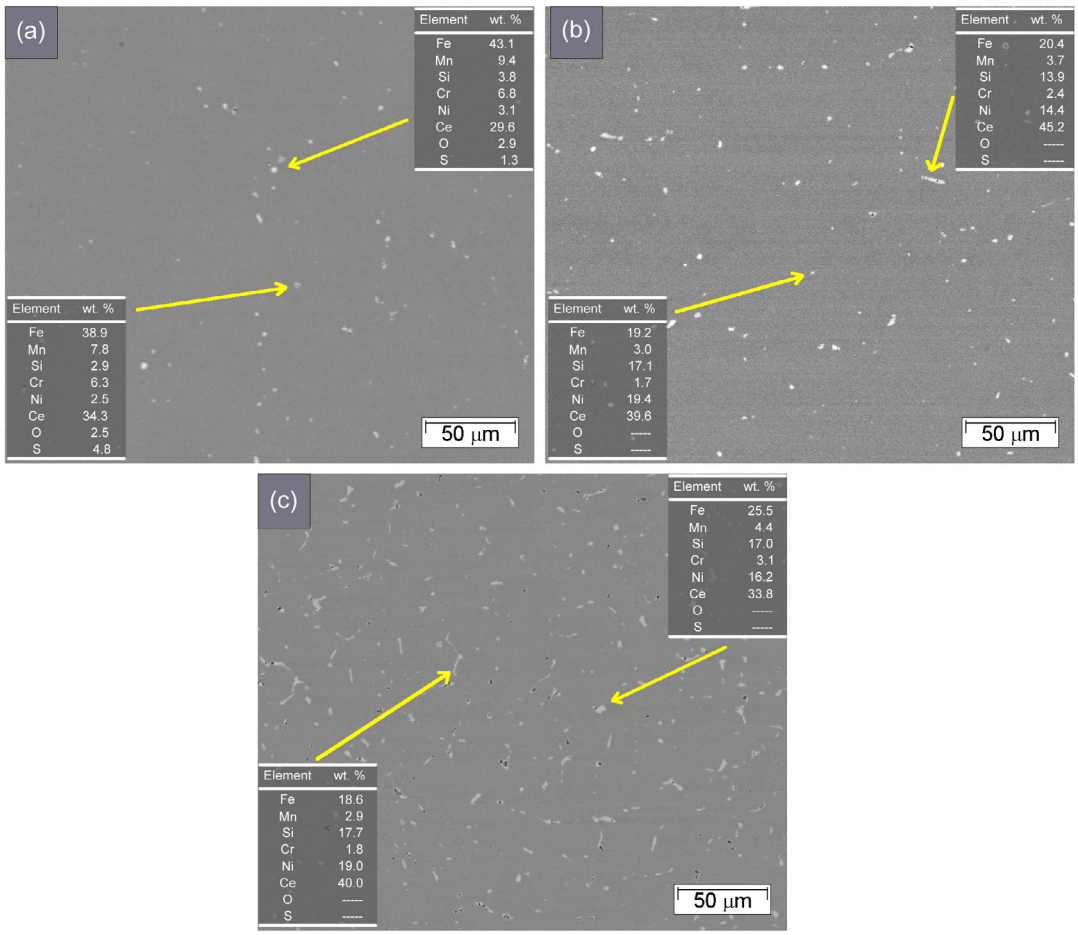

Figure 3. BSE–SEM images showing the distribution and morphology of Ce-rich particles in the alloys: a) SMA-2, b) SMA-3, and c) SMA-4.

variations in chemical composition. In SMAs 3 and 4, the particles formed are Ce rich with high Si and Ni contents and no measurable O and S contents, suggesting that they are intermetallic compounds.

Figure 4 shows grain boundary maps of the SMAs from the EBSD analyses. The mean grain size values, grain boundary density (total high-angle grain boundary length over the analyzed area), and annealing twin density (total twin boundary length over the analyzed area) for all alloys are given in **Table 2**. It is observed that the addition of Ce leads to a decrease in grain size accompanied by a significant increase in grain boundary densities and annealing twins. From Figure 4, it can also be seen that the ε-martensite regions (highlighted in black) are more homogeneous and finely distributed in alloy SMA-3 compared to SMAs 1, 2, and 4. Regarding the strengthening of the austenite phase promoted by grain refinement and second-phase hardening, the hardness remained unchanged with the addition of 0.18 wt% Ce, retaining about 216 HV, and increased to 230 HV with the addition of 0.42 wt% Ce, followed by a slight decrease with the addition of 0.96 wt% Ce (about 225 HV), as shown in **Figure 5**.

2.2. Transformation Temperatures and Phase Volume Fraction

DSC thermograms are shown in **Figure 6**, where the peaks of maximum values represent exothermic reactions, (i.e., γ-austenite → ε-martensite on cooling) and the minima represent endothermic reactions (in this case the reverse ε-martensite → γ-austenite occurring on heating). As shown in **Table 3**, the mean temperatures of A_S, A_F, and M_F are close to the experimental error observed for each of the alloys and show no tendency to increase or decrease with the addition of Ce. This indicates that these temperatures are not affected by the Ce addition. On the other hand, the M_S temperature increases with Ce additions. From Table 3, it can be seen that the mean M_S temperature value for the SMA-1 is above room temperature (≈36 °C) and increases by about 6 °C with the 0.18 wt% Ce addition (SMA-2). For SMA-3, an increase in M_S temperature of about 24 °C is observed compared to SMA-1, which remains unchanged with the addition of 0.96 wt% Ce (SMA-4). The increase in M_S temperature with Ce additions indicates that the amount of thermal ε-martensite in the microstructure tends to increase with Ce additions.

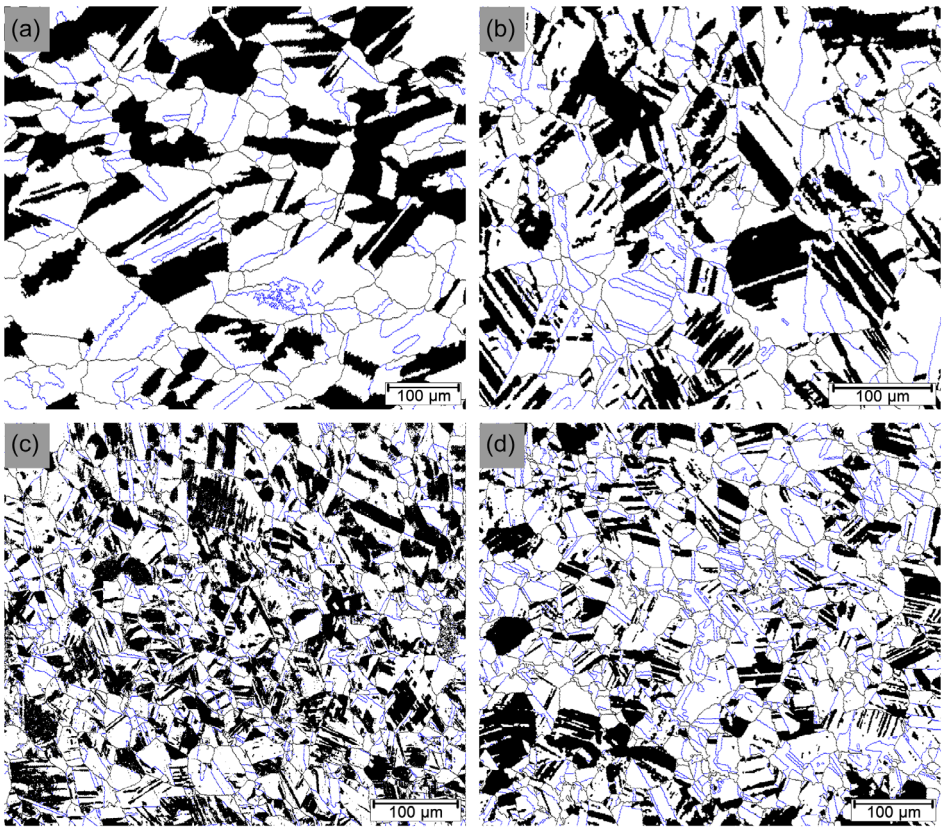

Figure 4. Grain boundary maps from SEM–EBSD analyses of: a) SMA-1, b) SMA-2, c) SMA-3, and d) SMA-4. High-angle grain boundaries (austenite) are black lines (15–62°) and annealing twin boundaries are blue lines (62–65°). ε-martensite regions are in black.

Table 2. Mean austenitic grain size and density of grain boundaries and annealing twins obtained from EBSD analysis.

Material	Average grain size [μm]	Density of grain boundaries [cm^{-1}]	Density of annealing twins [cm^{-1}]
SMA-1	92 ± 19	377	193
SMA-2	38 ± 13	644	374
SMA-3	23 ± 13	956	453
SMA-4	23 ± 9	1079	534

Figure 7 shows the XRD patterns of the SMAs as a function of Ce content after solution treatment and water quenching. Crystalline peaks of γ-austenite and ε-martensite are observed in all samples. Other peaks that are related to the inclusion of Ce-rich oxysulfide, and/or intermetallic phases are not detected in the XRD patterns. As shown in **Table 4**, the volume fractions of the phases estimated by quantitative Rietveld phase analysis indicate that the volume fraction of thermal ε-martensite increases with Ce addition, which is related to the increase in M_S temperature.

2.3. Shape Memory Behavior

Figure 8 shows the results of the bending tests with the contributions of the ESR and SMR components that result in the TSR.

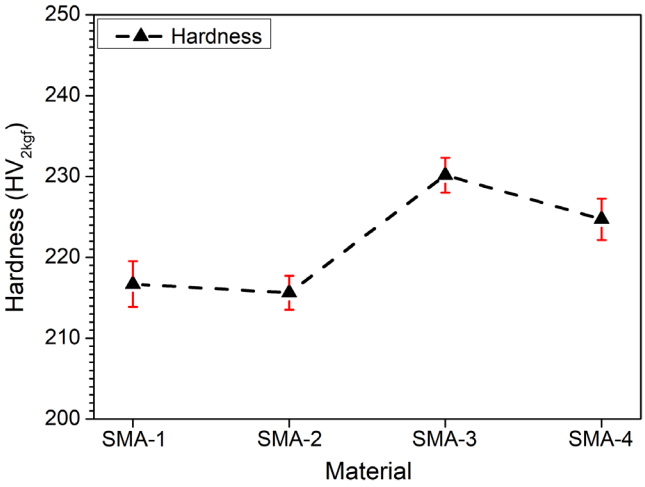

Figure 5. Average hardness as a function of Ce content.

A significant increase in TSR is observed with 0.18 and 0.42 wt% Ce additions compared to SMA-1. On the other hand, the addition of 0.96 wt% Ce promotes a significant reduction in the shape recovery to a lower value (about 67%) than that observed for SMA-1 (about 72%). Comparing the beneficial effect of the addition of Ce on the improvement of the TSR, it is observed that 0.42 wt% gives the highest TSR (about 92%), that is, a return

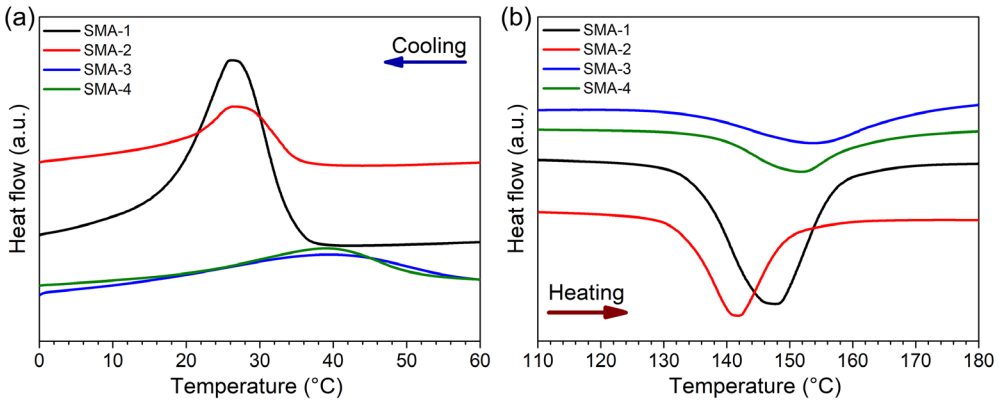

Figure 6. Change in transformation temperatures with the Ce addition: a) γ-austenite → ε-martensite on cooling and b) reverse ε-martensite → γ-austenite transformation on heating.

Table 3. Phase transformation temperatures determined from DSC curves.

Material	Phase transformation temperature [°C]			
	M_S	M_F	A_S	A_F
SMA-1	36 ± 1	16 ± 2	136 ± 2	159 ± 2
SMA-2	42 ± 1	23 ± 3	129 ± 4	154 ± 1
SMA-3	60 ± 1	17 ± 1	133 ± 2	168 ± 1
SMA-4	57 ± 3	20 ± 3	135 ± 3	165 ± 3

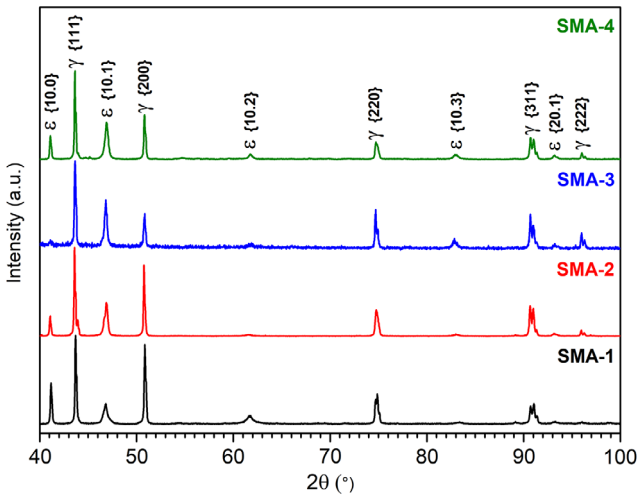

Figure 7. XRD patterns of the microstructure of SMA 1, SMA 2, SMA 3, and SMA 4.

Table 4. Volume fraction of the γ-austenite and thermal ε-martensite phases after solution treating and water quenching.

Material	Phase	Volume fraction [%]
SMA-1	γ-austenite	63
	ε-martensite	37
SMA-2	γ-austenite	57
	ε-martensite	43
SMA-3	γ-austenite	58
	ε-martensite	42
SMA-4	γ-austenite	52
	ε-martensite	48

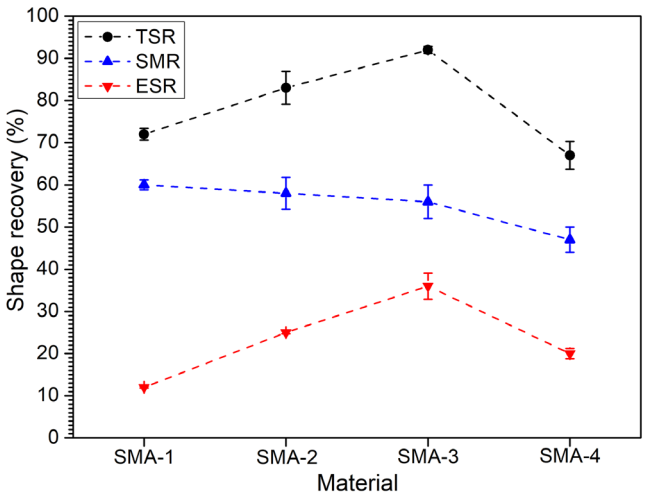

Figure 8. The TSR of the SMAs and the respective contributions of the ESR and the SMR to the TSR as a function of the Ce content.

of 3.7% with respect to the 4% PS. Figure 8 also shows that the observed TSR of about 72% for SMA-1 is mainly due to the SME, with the contribution of the SMR and ESR components to the TSR being about 83% and 17%, respectively. For the alloys with 0.18 and 0.42 wt% Ce additions, the contribution of SMR decreases while that of ESR increases significantly. The 83% TSR observed for SMA-2 is composed of 70% SMR and 30% ESR, whereas the 92% TSR obtained for SMA-3 is composed of 61% SMR and 39% ESR. For SMA-4, the lower TSR obtained (≈67%) is the result of 70% SMR and 30% ESR contributions.

These results show that the improvement in TSR obtained by the addition of Ce is due to the increased contribution of ESR to TSR, while that of SMR decreased.

3. Discussion

The Ce addition in the austenitic Fe–13.50Mn–3.98Si–9.54Cr–4.51Ni SMA contributed to the improved TSR, resulting in almost complete recovery after 4% PS with 0.42 wt% Ce addition. The magnitudes of shape recovery achieved with Ce additions of 0.18 and 0.42 wt% are higher than those previously reported under similar conditions of the processing route (casting, annealing and rolling) without thermomechanical training. Zhao et al.[6,13] reported values of 72% of TSR in an Fe–16Mn–5Si–8Cr–5Ni–0.3Ce alloy with 2.1% PS at room temperature and 1000 °C solution treatment and 91% with 700 °C solution treatment. In both studies, the authors reported that Ce played a more significant role in improving SME than N and Ti. In another study of REE additions, Huang et al.[12] who investigated the effect of adding a La and Ce blend (with more La than Ce) in the range from 0.03 to 0.46 wt% on the TSR of Fe–24.60Mn–6.44Si–5.34Cr alloy, observed a TSR value of 80% after 4% PS with the addition of 0.16 wt% of the blend and a subsequent decrease in TSR with the addition of 0.46 wt%. However, higher values of TSR were achieved after performing thermomechanical training cycles.

On the other hand, comparing the results with a conventional SMA without any alloying element addition, Li et al.[28] reported a low value of 60% of the TSR for Fe–13Mn–5Si–10Cr–6Ni annealed at 1000 °C with about 4% PS at room temperature. Other authors have published SME experiments with the formation of second-phase particles after aging treatment and also showed lower TSR values than Ce (or other REE) addition, such as Dong et al.[8] who reported 72% of TSR in Fe–17Mn–5Si–10Cr–4Ni–1(V,C) after aging at 850 °C and 4% PS at room temperature. These results indicate that, under the same experimental conditions, the addition of Ce (or a mixture of Ce and La) was responsible for a higher shape recovery ratio than the base Fe–Mn–Si–Cr–Ni composition and higher than alloys with second-phase precipitates, where aging treatment is required to achieve maximum TSR. Two very common ways to increase the shape recovery are thermomechanical training[26,29] and PS at low temperatures,[6,8] achieving TSR values above 90%. In this study, it is shown that it is possible to achieve similar values simply by adding Ce, without the need for complex and expensive processing methods.

The discussion begins with an analysis of the changes in microstructure, mechanical strength, and amount of thermal ε-martensite promoted by the addition of Ce. Subsequently, the effects of Ce on the SMR and ESR contributions to the TSR are discussed. These effects are elucidated by analyzing the microstructure of SMA-1, SMA-3, and SMA-4 after 4% PS. The analysis of the microstructure of SMA-2 after 4% PS was not considered because the increase in TSR with the addition of 0.18 wt% Ce occurs in the same manner as that observed for SMA-3.

3.1. Effect of Ce on Microstructure, Mechanical Strength, and Thermal ε-Martensite

Ce has low solubility in Fe-based alloys, so the last liquid to solidify between grains is enriched in Ce, leading to the formation of Ce-rich particles, which are formed by peritectic reaction.[30,31] These particles typically have significant O and S contents due to the high affinity of Ce for these elements,[32] acting as scavengers for these elements and promoting the purity of the alloys. As a result, much of the Ce added to the alloy becomes Ce-rich particles, causing grain boundary pinning that promotes significant austenitic grain size reduction (Table 2).[12] This grain refinement resulted in an increase in grain boundary density and annealing twins. Both grain refinement and the formation of Ce-rich particles contributed to the strengthening of the austenite phase at 0.42 wt% Ce addition (Figure 5). However, the addition of 0.96 wt% Ce resulted in the formation of large Ce-rich particles which caused softening of the metallic matrix compared to SMA-3.

Considering a previous study[33] which reported that M_S temperature decreases with grain refinement due to austenite stabilization promoted by matrix strengthening, the increase in M_S temperature with the addition of Ce to the alloy (Table 2) can be an indication of the reduction in SFE.[34] This facilitates overlapping SFs, which act as nucleation embryos for ε-martensite, resulting in an increase in M_S temperature and consequently an increase in the amount of thermal ε-martensite. The decrease in SFE with Ce additions may be related to the increased amount of Si in the Ce-rich particles (Figure 3), which is known to decrease SFE,[11,35,36] since the contribution of Ce in reducing SFE is limited by its negligible solubility in the alloy.

Recent studies have shown that precipitates can facilitate the formation of numerous SFs in austenitic phase.[37] This phenomenon occurs due to dislocation dissociation at the matrix–precipitate interface, which adjusts the elastic strain field.[38,39] As a result, the newly formed dislocations may experience a decrease in the local SFE in the presence of Ce-rich particles with high Si content, leading to a reduction in the overall SFE of the alloys with Ce addition. Khodaverd et al.[37] suggested that the change in the local chemical composition of the austenite surrounding the precipitates and the lattice strain during their formation may play a key role in the formation of the SF and the increase in the M_S temperature.

To understand the effect of Ce content on phase transformation temperatures and SF mechanisms on ε-martensite nucleation, SFE values for SMAs 1, 3 and 4 were estimated by XRD line profile analysis. The SF probability (α) and the rms microstrain in the <111> direction (ϵ^2_{50111}) were used to determine the relative SFE values. Since SFs occur on the (111) close-packed planes in an FCC crystal, the results of the shift of the diffraction lines can be used to estimate α. In this case, a comparison between the XRD patterns of ST and 4% PS samples, shown in **Figure 9**, gives a good estimate of α, which is also related to the number of ε-martensite nuclei per volume of austenite. According to the Schramm and Reed,[35] α can be calculated from Equation (4):

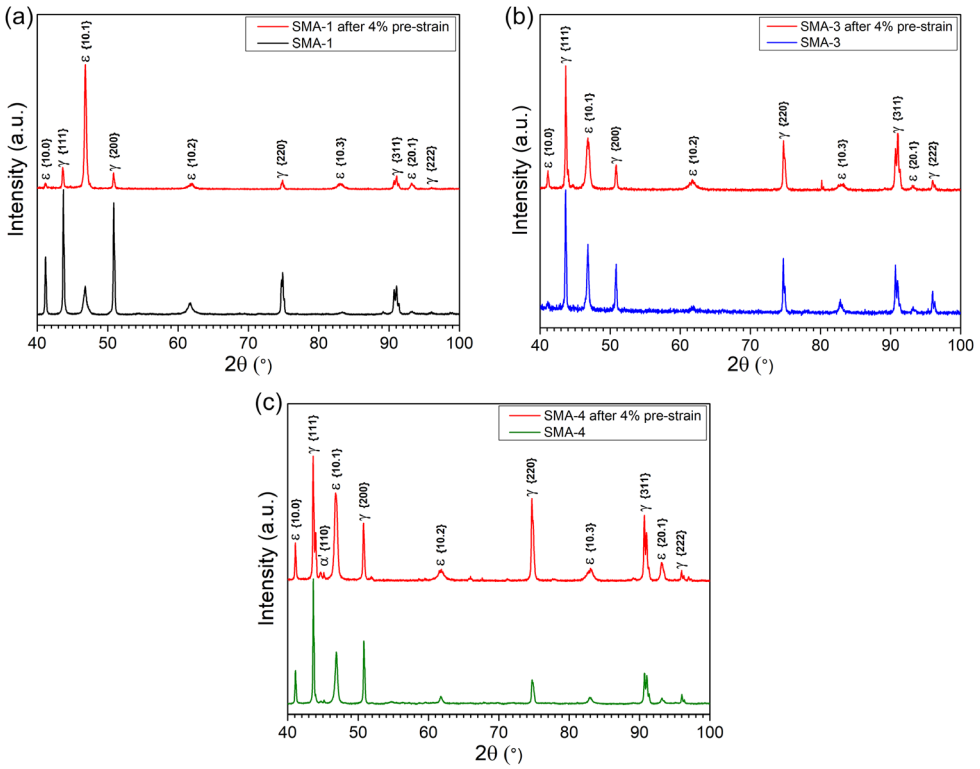

Figure 9. Comparison between the XRD patterns of the microstructure of the ST samples and the samples with 4% PS after solution treatment: a) SMA-1, b) SMA-3, and c) SMA-4.

$$\Delta 2\theta = (2\theta_{200} - 2\theta_{111})_{4\%\,PS} - (2\theta_{200} - 2\theta_{111})_{ST} = -\frac{45\sqrt{3}}{\pi^2}\left(\tan\theta_{200} + \frac{1}{2}\tan\theta_{111}\right)\alpha \quad (4)$$

where 2θs are the peak positions in degrees.

To determine the microstrain (ε) and crystallite size (D), the Williamson-Hall (W–H) method was used,[40] as shown in Equation (5).

$$\beta\cos\theta = \varepsilon 4\mathrm{sen}\theta + \frac{K\lambda}{D} \quad (5)$$

β is the full width at half maximum (FMWH), K is a constant equal to 0.9, and θ is the peak position.

Prior to W–H analysis, for all profiles, the instrumental peak magnification was subtracted from the peak widths according to Cagliotti's equation[41] based on measurements of the diffraction pattern of a high-purity Si standard powder sample. In addition, the reflections of each diffraction peak were fitted with a Gaussian function to obtain the peak position and FMWH values. The microstrain values for each alloy were then converted to (ε^2_{50111}) values using the method described by Klug and Alexander.[42]

The relative SFE (γ) can be calculated from Equation (6).[35]

$$\gamma = \frac{K_{111}\omega_o G_{111} a_0 A^{-0.37}\varepsilon^2_{50111}}{\alpha\pi\sqrt{3}} \quad (6)$$

where $K_{111}\omega_o$ is a proportional constant equal to 6.6. G_{111} is the shear modulus in the (111)α plane determined from the Young's modulus measured by nanoindentation (Figure S1, Supporting information) using the Oliver–Pharr method,[43] and the values obtained were converted to shear modulus values assuming that the alloys are isotropic. Poisson's coefficient is 0.25. a_0 is the lattice parameter of the ST sample. A is the Zener anisotropy determined by the elastic stiffness coefficients C_{11}, C_{12}, and C_{44}: $A = 2C_{44}/(C_{11}-C_{12})$. In this work, the following stiffness coefficients were used $C_{11} = 218$ GPa, $C_{12} = 129$ GPa, and $C_{44} = 79$ GPa.[35] **Table 5** shows the main XRD parameters for SMAs 1, 3, and 4 and their relative SFE values.

From Table 5, it can be seen that the SFE value for SMA-1 is about 26.4 mJ m^{-2}. This value is similar to that estimated by Maji et al.[11] for the conventional Fe–14Mn–9Cr–5Si–5Ni SMA from XRD line profile analysis, between 25 and 30 mJ m^{-2}. With the addition of 0.42 wt% Ce (SMA-3), the SFE value decreased to 10.2 mJ m^{-2}, indicating that the increase in M_S temperature is

Table 5. Parameters used to determine SFE values and volume fractions of phases estimated by quantitative Rietveld phase analysis for SMAs 1, 3, and 4.

Material	α	γ/G_{111}	γ [mJ m^{-2}]	G [Pa]	γ [%]	ε [%]
SMA-1	2.22×10^{-4}	2.82×10^{-13}	26.4	9.36×10^{10}	23	77
SMA-3	4.59×10^{-5}	1.04×10^{-13}	10.2	9.84×10^{10}	38	62
SMA-4	2.27×10^{-4}	2.52×10^{-13}	25.8	1.02×10^{11}	36	64

related to the decrease in SFE, probably caused by the formation of Ce-rich particles with high Si content. However, the SFE value does not decrease significantly compared to SMA-1 with the addition of 0.96 wt% Ce (25.8 mJ m^{-2}). This result seems to be related to a competition caused by the decrease of SFE in regions where Ce-rich particles with high Si content were formed and there was increase of SFE promoted by Si depletion in regions adjacent to these particles. Since the number of Ce-rich particles formed in SMA-4 is greater than that in SMA-3 (Figure 3), the greater the Si depletion in the austenite. As a result, the SFE does not decrease significantly with the addition of 0.96 wt% Ce. Nevertheless, this small decrease in SFE was apparently sufficient to increase the M_S temperature of SMA-4 (Table 3). It is important to mention that the increase in SFE in Si-depleted regions may have reached values that activate twinning as a deformation mechanism,[44] contributing to the higher density of annealing twins observed in SMA-4 (Table 2).

3.2. Effect of Ce on SMR and ESR Contributions to TSR

In SMA-1, the TSR was almost entirely due to the contribution of the SMR (Figure 8). The stress-induced martensite volume fraction ($\Delta_\varepsilon = V_{\varepsilon 4\%} - V_{\varepsilon T}$) estimated by quantitative Rietveld phase analysis from the XRD pattern of SMA-1 after 4% PS (Figure 9) was about 40%, leaving about 23% of the austenite phase that did not undergo phase transformation. In this alloy, the low shape return achieved (2.9%) can be attributed to two factors: 1) The first factor is the high volume fraction of pre-existing thermal ε-martensite in the microstructure of the material (37%), which reduces the amount of austenite available to undergo phase transformation during PS.[45] In addition, this thermal ε-martensite does not cause a shape change of the sample (or component) as it is self-accommodating; 2) The large number of ε-martensite plates of different variants observed within the coarse austenitic grains, intersecting each other (Figure 2a), preventing the growth of ε-martensite plates during PS, as shown in **Figure 10**a, is another factor. It has been mentioned[46] that such a condition can cause the strains generated by different ε-martensite variants to cancel each other out to a certain point, resulting in a reduction in the total strain. This results in both stress-induced ε-martensite and dislocation slip, the latter being detrimental to SME.

For SMAs 2 and 3, the increase in the ESR contribution was responsible for the improvement in TSR with Ce additions of 0.18 and 0.42 wt%. In these alloys, monovariant ε-martensite plates were formed within austenitic grains, which could be due to the formation of Ce-rich particles. It has been suggested[37] that precipitates promote the formation of SFs grouped along the same orientation within austenitic grains instead of randomly oriented SFs, which favors the formation of monovariant ε-martensite plates. Although the formation of monovariant ε-martensite plates in combination with the strengthening of the austenitic phase with 0.42 wt% Ce and a lower SFE of 12 mJ m^{-2} is considered the ideal approach to achieve better SME,[8,44,46] the stress-induced martensite volume fraction was half that observed for SMA-1 (about 20%). This can be attributed to both grain refinement, which has increased the density of grain boundaries and annealing twins, and the formation of Ce-rich particles.

In Fe–Mn–Si-based SMAs, it has been reported[46] that during PS, ε-martensite tips tend to interact with barriers such as other ε-martensite variants, α′-martensite, dislocations, grain boundaries, and annealing twins. As a result, the partials located in the ε-martensite tips can become trapped in these barriers and prevented from moving during heating. This in turn requires the nucleation of new partials during heating to achieve reverse martensitic transformation, and the Burgers vectors of these newly formed partials can be primarily randomly oriented. Consequently, the Burgers vectors of the newly formed partials will not be antiparallel to those of their counterparts acting in the martensitic transformation, promoting a reduction in SME. Therefore, it is plausible that the decrease in the SMR contribution to the TSR with the addition of Ce is partly due to the increased density of grain boundaries and annealing twins. In this case, since SMA-4 has the highest density of grain boundaries and annealing twins, the contribution of SMR to the TSR is lowest for this alloy, as evidenced by the lowest stress-induced martensite volume fraction (about 16%).

It is worth noting that the highest volume fraction of ε-martensite in SMA-4, about 48% (Table 4), may also have contributed to the lowest volume fraction of strain-induced martensite. It is well known that a high thermal ε-martensite volume fraction can promote in the formation of α'-martensite during PS.[11] This phase was visible in the XRD pattern of the microstructure of SMA-4 after 4% PS (Figure 9c). The formation of this phase is related to the coalescence of the pre-existing thermal ε-martensite with the reorientation process during PS, leading to the formation of α'-martensite at the intersection of the

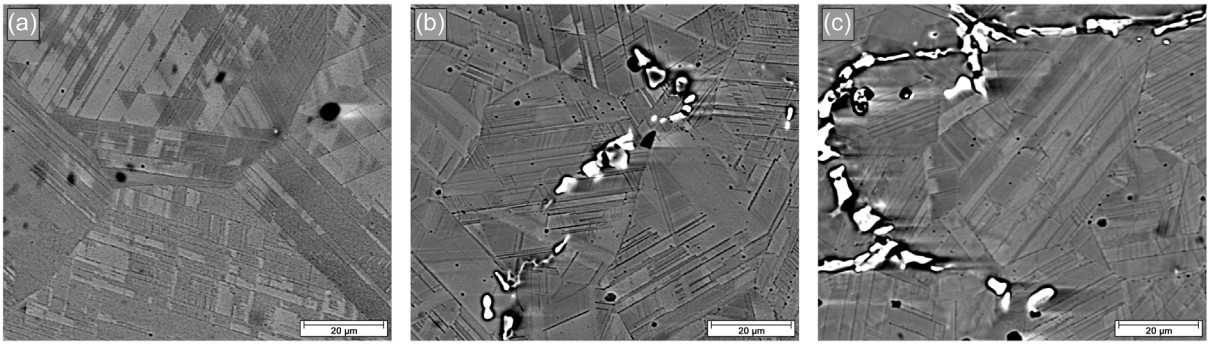

Figure 10. BSE–SEM images of the microstructures of SMAs 1, 3, and 4 after 4% PS: a) SMA-1, b) SMA-3, and c) SMA-4.

ε-martensite plates, preventing the formation of further ε-martensite on loading and its reversal on heating.[47,48] Although the volume fraction of α'-martensite quantified by the Rietveld phase analysis was very low (about 1%), the fact that this phase is formed in the microstructure of SMA-4 during PS also contributes to its lower SME.

As for the Ce-rich particles, they were obstacles to the growth of ε-martensite plates within the grain, as shown for SMA-3 in Figure 10b. It has been proposed[7,19,49] that the pinning effect induced by precipitated particles over ε-martensite plates during stress-induced martensitic transformation creates a local back-stress effect, where the stress fields facilitate the reverse movement of Shockley partial dislocations, leading to a $\varepsilon \rightarrow \gamma$ transformation immediately after unloading, resulting in a macroscopic volume change. Thus, the contribution of the ESR to the TSR increases with the number of Ce-rich particles, which is consistent with the highest ESR observed for SMA-3. In the case of SMA-4, the effect of back stress was less pronounced due to the fact that most of the Ce-rich particles are preferentially formed at grain boundaries, as shown in Figure 10c. In addition, the high added Ce content resulted in the formation of large Ce-rich particles, leading to a decrease in the interfacial area between the matrix and the precipitates.

4. Conclusion

Based on the results, the following conclusions can be drawn: 1) Ce additions promoted the formation of Ce-rich particles, which caused grain refinement. At 0.42 wt% Ce addition, both grain refinement and the formation of Ce-rich particles contributed to the strengthening of the austenitic phase; 2) the M_S temperature increased with Ce additions due to a reduction in SFE, which was significantly reduced with the addition of 0.42 wt% Ce. This reduction was promoted by the formation of Ce-rich particles with high Si content in the microstructure. However, no significant reduction in SFE was observed with the addition of 0.96 wt% Ce. This seems to be related to a competition caused by the decrease in SFE in regions where Ce-rich particles with high Si content were formed and the increase in SFE promoted by Si depletion in regions adjacent to these particles; 3) the SMR component decreases with Ce addition, while the ESR component follows the trend of the TSR, increasing with Ce additions of 0.18 and 0.42 wt%, with a significant decrease at 0.96 wt% Ce addition; 4) the increase in the ESR component with Ce additions of 0.18 and 0.42 wt% is attributed to the formation of Ce-rich particles within the grain that act as pinning sites over ε-martensite plates and promote reverse transformation from ε-martensite to γ-austenite upon unloading; and 5) the decrease in SME with the addition of Ce is attributed to grain refinement, promoting an increase in the density of grain boundaries and annealing twins, which act as barriers to martensitic transformation.

Supporting Information

Supporting Information is available from the Wiley Online Library or from the author.

Acknowledgements

The authors gratefully acknowledge PPGCEM/UFSCar (Postgraduate Program in Materials Science and Engineering of the Federal University of São Carlos) and the Brazilian research-funding agency CNPq (National Council for Scientific and Technological Development, grant nos. 460659/2014-6 and 312614/2020-9) for the financial support of this work. The permission granted to authors to utilize the facilities of the Laboratory of Structural Characterization (LCE/DEMa/UFSCar) is also greatly appreciated. This study was financed in part by the Coordenação de Aperfeiçoamento de Pessoal de Nível Superior - Brasil (CAPES) - Finance Code 001.

Conflict of Interest

The authors declare no conflict of interest.

Data Availability Statement

The data that support the findings of this study are available from the corresponding author upon reasonable request.

Keywords

austenitic Fe–Mn–Si–Cr–Ni shape memory alloys, Bend tests, Cerium, Microstructures

Received: September 18, 2023
Revised: December 6, 2023
Published online: December 22, 2023

[1] R. Silva, G. S. Vacchi, I. G. R. Santos, A. M. de Sousa Malafaia, C. L. Kugelmeier, A. A. Mendes Filho, C. Pascal, V. L. Sordi, C. A. D. Rovere, *Corros. Sci.* **2020**, *163*, 108269.
[2] A. Sato, E. Chishima, K. Soma, T. Mori, *Acta Metall.* **1982**, *30*, 1177.
[3] H. Otsuka, H. Yamada, T. Maruyama, H. Tanahashi, S. Matsuda, M. Murakami, *ISIJ Int.* **1990**, *30*, 674.
[4] S. M. H. Otsuka, M. Murakami, in *MRS Int. Meeting on Advanced Materials, 1st, Proc. Vol. 9 - Shape Memory Materials*, Tokyo, Japan, May–June **1988**.
[5] S. Kajiwara, *Mater. Sci. Eng., A* **1999**, *273–275*, 67.
[6] C. Zhao, *Metall. Mater. Trans. A* **1999**, *34*, 2599.
[7] S. Kajiwara, D. Liu, T. Kikuchi, N. Shinya, *Scr. Mater.* **2001**, *44*, 2809.
[8] Z. Dong, U. E. Klotz, C. Leinenbach, A. Bergamini, C. Czaderski, M. Motavalli, *Adv. Eng. Mater.* **2009**, *11*, 40.
[9] K. Li, Z. Dong, Y. Liu, L. Zhang, *Smart Mater. Struct.* **2013**, *22*, 045002.
[10] N. Stanford, D. P. Dunne, *J. Mater. Sci.* **2006**, *41*, 4883.
[11] B. C. Maji, M. Krishnan, Gouthama, R. K. Ray, *Metall. Mater. Trans. A* **2011**, *42*, 2153.
[12] X. Huang, Y. Lei, B. Huang, S. Chen, T. Y. Hsu, *Mater. Lett.* **2003**, *57*, 2787.
[13] C. Zhao, G. Liang, C. Li, Z. Jin, *Scr. Mater.* **1998**, *38*, 1163.
[14] H. Suzuki, *J. Phys. Soc. Jpn.* **1962**, *17*, 322.
[15] E. Cadel, A. Fraczkiewicz, D. Blavette, *Scr. Mater.* **2004**, *51*, 437.
[16] I. Fartushna, A. Khvan, A. Dinsdale, V. Cheverikin, D. Ivanov, A. Kondratiev, *J. Alloys Compd.* **2016**, *654*, 424.
[17] G. Wang, H. Peng, C. Zhang, S. Wang, Y. Wen, *Smart Mater. Struct.* **2016**, *25*, 075013.
[18] L. Yong, Q. Luo, H. Peng, J. Yan, B. Xu, Y. Wen, *Mater. Charact.* **2020**, *169*, 110650.

[19] K. A. Käfer, H. H. Bernardi, O. de S. Santos, L. Otubo, N. B. de Lima, J. Otubo, *Mater. Res.* **2018**, *21*, e20170958.
[20] K. A. Käfer, H. H. Bernardi, L. K. F. Naito, N. B. de Lima, J. Otubo, *Mater. Sci. Forum* **2013**, *738–739*, 496.
[21] R. Silva, D. J. Young, C. B. M. Junior, G. S. Vacchi, C. A. T. Alberto, A. M. de S. Malafaia, C. Pascal, C. A. D. Rovere, *Corros. Sci.* **2022**, *209*, 110788.
[22] L. F. S. Baroni, R. Silva, G. S. Vacchi, V. L. Sordi, C. A. D. Rovere, *Mater. Today Commun.* **2020**, *25*, 101649.
[23] R. A. Shakoor, F. A. Khalid, *Mater. Sci. Eng., A* **2009**, *499*, 411.
[24] B. H. Toby, R. B. Von Dreele, *J. Appl. Crystallogr.* **2013**, *46*, 544.
[25] M.-M. Pan, X.-M. Zhang, D. Zhou, R. D. K. Misra, P. Chen, *Mater. Sci. Eng., A* **2020**, *797*, 140107.
[26] A. Akhondzadeh, K. Zangeneh-Madar, S. M. Abbasi, *Mater. Sci. Eng., A* **2008**, *489*, 267.
[27] J. H. Yang, H. Chen, C. M. Wayman, *Metall. Trans. A* **1992**, *23*, 1431.
[28] H. Li, D. Dunne, N. Kennon, *Mater. Sci. Eng., A* **1999**, *273–275*, 517.
[29] J. Otubo, P. Mei, S. Koshimizu, A. Shinohara, C. Suzuki, *Mater. Sci. Eng., A* **1999**, *273–275*, 533.
[30] M. Mardani, I. Fartushna, A. Khvan, V. Cheverikin, A. Dinsdale, *J. Alloys Compd.* **2019**, *781*, 524.
[31] X. Su, J.-C. Tedenac, *Calphad* **2006**, *30*, 455.
[32] F. Pan, J. Zhang, H.-L. Chen, Y.-H. Su, Y.-H. Su, W.-S. Hwang, *Sci. Rep.* **2016**, *6*, 35843.
[33] S. Kajiwara, *Metall. Trans. A* **1986**, *17*, 1693.
[34] W. Zhou, B. Jiang, X. Qi, T. Hsu (Xu Zuyao), *Scr. Mater.* **1998**, *39*, 1483.
[35] R. E. Schramm, R. P. Reed, *Metall. Trans. A* **1975**, *6*, 1345.
[36] J. C. Li, M. Zhao, Q. Jiang, *Metall. Mater. Trans. A* **2000**, *31*, 581.
[37] H. Khodaverdi, M. Mohri, A. S. Ghorabaei, E. Ghafoori, M. Nili-Ahmadabadi, *Mater. Charact.* **2023**, *195*, 112486.
[38] H. Khodaverdi, M. Mohri, E. Ghafoori, A. S. Ghorabaei, M. Nili-Ahmadabadi, *J. Mater. Res. Technol.* **2022**, *21*, 2999.
[39] R. Shi, N. Ma, Y. Wang, *Acta Mater.* **2012**, *60*, 4172.
[40] G. K. Williamson, W. H. Hall, *Acta Metall.* **1953**, *1*, 22.
[41] G. Caglioti, A. Paoletti, F. P. Ricci, *Nucl. Instrum.* **1958**, *3*, 223.
[42] L. E. A. Harold, P. Klug, *X-ray Diffraction Procedures: for Polycrystalline and Amorphous Materials*, 2nd Revised ed., Wiley-Interscience, Hoboken, NJ **1974**.
[43] W. C. Oliver, G. M. Pharr, *J. Mater. Res.* **1992**, *7*, 1564.
[44] H. Peng, G. Wang, S. Wang, J. Chen, I. MacLaren, Y. Wen, *Mater. Sci. Eng., A* **2018**, *712*, 37.
[45] J. H. Jun, W. Jin, C. S. Choi, *Scr. Metall. Mater.* **1995**, *33*, 1339.
[46] M. J. Lai, Y. J. Li, L. Lillpopp, D. Ponge, S. Will, D. Raabe, *Acta Mater.* **2018**, *155*, 222.
[47] J. H. Yang, C. M. Wayman, *Metall. Trans. A* **1992**, *23*, 1445.
[48] B. C. Maji, M. Krishnan, *Scr. Mater.* **2003**, *48*, 71.
[49] C. Leinenbach, A. Arabi-Hashemi, W. J. Lee, A. Lis, M. Sadegh-Ahmadi, S. Van Petegem, T. Panzner, H. Van Swygenhoven, *Mater. Sci. Eng., A* **2017**, *703*, 314.